Received September 28, 2021, accepted October 26, 2021, date of publication October 28, 2021, date of current version November 8, 2021.

Digital Object Identifier 10.1109/ACCESS.2021.3124019

Automatic Polyp Detection Using Microwave Endoscopy for Colorectal Cancer Prevention and Early Detection: Phantom Validation

ALEJANDRA GARRIDO[1], ROBERTO SONT[1], WALID DGHOUGHI[1], SERGI MARCOVAL[1], JORDI ROMEU[2], (Fellow, IEEE), GLÒRIA FERNÁNDEZ-ESPARRACH[1,3], IGNASI BELDA[1], AND MARTA GUARDIOLA[1]

[1]MiWEndo Solutions, 08014 Barcelona, Spain
[2]CommSensLab, Universitat Politècnica de Catalunya (UPC), 08034 Barcelona, Spain
[3]Endoscopy Unit, Department of Gastroenterology, Hospital Clínic, CIBEREHD, IDIBAPS, University of Barcelona, 08036 Barcelona, Spain

Corresponding author: Marta Guardiola (marta@miwendo.com)

The work of Alejandra Garrido was supported by DIN2019-010857. The work of Roberto Sont, Ignasi Belda, and Marta Guardiola was supported in part by the European Union's Horizon 2020 Research and Innovation Programme under Grant 960251 and in part by the European Institute of Innovation and Technology (EIT). The work of Jordi Romeu was supported by PID2019-107885GB-C31/AEI/10.13039/501100011033.

ABSTRACT A system to integrate microwave imaging with optical colonoscopy is presented. The overarching goal is to improve the prevention and early diagnosis of one of the main health and economic burdens of an increasingly aging population, i.e., colorectal cancer. For a colonoscopy, the gold standard for colorectal cancer diagnosis, 22% of polyps are not detected, and the risk of cancer after a negative colonoscopy can be up to 7.9%. To remedy this, a microwave imaging system able to generate an alarm when a polyp is detected is designed, manufactured and validated with a colon phantom composed of tissue-mimicking oil-gelatin materials reproducing the anatomy and dielectric properties of a human colon with a polyp. The acquisition was performed by a miniaturized ring-shaped switched array of 16 antennas attachable at the tip of a conventional colonoscope. This has been conceived to satisfy endoscopy size restrictions, patient safety and intercompatibility with current clinical practice. A Modified Monofocusing imaging method preceded by a previous frame average subtraction as a calibration technique shows a perfect detection of a 10-mm polyp (100% sensitivity and specificity) in the eight analyzed trajectories. The phantom results demonstrate the feasibility of the system in future preclinical trials.

INDEX TERMS Backpropagation algorithms, endoscopes, medical diagnostic imaging, microwave antenna arrays, microwave imaging.

I. INTRODUCTION

Globally, 1.93 million new cases of colorectal cancer (CRC) are diagnosed annually, with 935,000 people dying from CRC in 2020 [1]. This has led to CRC being the second most common cause of cancer death in both men and women. CRC describes cancerous malignancies of the colon and rectum. Most cases of CRC begin as a growth of tissue, known as a polyp, which originates in the lining of the colon or rectum and grows in size over a period of several years. Polyps are common in patients over 50 years, but certain polyps (known as adenomas) are estimated to be precursors to 90% of CRC cases [2]. The overall five-year survival rate of CRC is approximately 65%, but drops to 14.3% if diagnosed at advanced stages, which is quite common given the absence of remarkable symptoms when the cancer is in a localized phase [3].

Large-scale studies have found that CRC can be cured in more than 90% of cases if adenomas are removed[2]. Optical colonoscopy is the most effective method for CRC diagnosis and is the only method that is able to remove polyps in the entire colon. During a colonoscopy, a long, flexible tube called a colonoscope is inserted into the rectum. A tiny video camera at the tip of the tube allows the doctor to view the

The associate editor coordinating the review of this manuscript and approving it for publication was Chulhong Kim.

This work is licensed under a Creative Commons Attribution 4.0 License. For more information, see https://creativecommons.org/licenses/by/4.0/

inside of the entire colon. However, the limited field of view of the camera (less than 180°), inadequate colon preparation and the subjectivity of the exploration dependent on the endoscopist's experience, among others, result in a polyp miss rate of 22% [4] and a risk of developing cancer after a negative colonoscopy, the so-called interval CRC of 8% [5].

In recent years, several devices and technologies have been developed to improve the detection rate of polyps such as high-definition endoscopes, endoscopes with multiple lenses (retrovision capability), and mucosal flattening accessories [6]. Chromoendoscopy, endoscopic microscopy (endocytoscopy and endomicroscopy) or hyperspectral techniques [7] are methods developed to magnify, enhance and estimate mucosal tissue and cell characteristics that can be linked to malignancy. All of these techniques are restricted to the optical information captured by the camera and increasingly require highly trained professionals. Because the outcomes of these methods are highly dependent on the operator's experience and human factors (fatigue, stress, resilience, etc.), a tool capable of automating the detection is needed. Artificial intelligence is increasingly used for the real-time assessment of endoscopic images [8]. However, if a lesion is not visualized by the camera, it cannot be detected by the algorithm. Studies indicate that 13.4% of the colon surface area might not be visualized during a standard colonoscopy [9], [10].

Microwave imaging allows us to scan 360° of the colon and automate detection. It has been developed for the last 40 years as a portable, non-ionizing, low-power, non-invasive, and low-cost medical diagnostic method [11] that is able to obtain anatomical and functional images of the interior of the human body based on the contrast in dielectric properties, i.e., the relative permittivity and the conductivity. Dielectric properties are biomarkers of many health problems, such as osteoporosis [12], heart infarction [13], pulmonary edema, etc., with breast cancer [14], [15] and brain stroke [16], [17] being the most researched and advanced topics. We recently demonstrated that the dielectric properties correlate with the malignancy grade of colon polyps [18]; the more similar to cancer, the higher the relative permittivity and conductivity. The results indicate that the maximum contrast between healthy mucosa and cancer was 30% and 90% for the relative permittivity and conductivity, respectively, at 8 GHz.

Table 1 shows how the proposed microwave endoscopy system compares with the gold standard, i.e., conventional colonoscopy, advanced colonoscopy techniques [6], mucosa flattening accessories [19] and deep learning-assisted colonoscopy [20]. The ADR, or Adenoma Detection Rate, is defined as the percentage of patients undergoing screening colonoscopy who have one or more adenomas detected and is the quality indicator of colonoscopy. ADR is not yet available for microwave endoscopy since it has not been used in humans so far. The ADR increase is measured with respect to a conventional colonoscopy.

This paper reports a system to integrate microwave imaging with optical colonoscopy aimed at improving the prevention and early detection of colorectal cancer. To the best of our knowledge, this is the first time that microwave imaging has been proposed for endoscopic applications. With the proposed system, the detection of polyps can be automatized by generating an alarm when a polyp is detected in order to warn the endoscopist. As the proposed system is an add-on to standard colonoscopy, if the alarm goes off and the polyp is not visualized with colonoscopy, then the doctor can better examine the area to find it. This feature will fill the gap between endoscopists with different levels of experience, which has been demonstrated to play an important role in colonoscopy effectiveness and moves forward a major trend of the automating medical explorations field.

TABLE 1. Performance comparison between different colon visualization methods.

Method	Field of view	Automatic detection	ADR increase
Conventional colonoscopy	<170°	No	-
High definition colonoscopy	<170°	No	4.5%
Magnification colonoscopy	<170°	No	0%
Chromoendoscopy	<170°	No	0%
Multi-lens colonoscopy	235°-360°	No	5%
Deep learning	- [1]	Yes	14%
Flattening accessories	<170°	No	16%
Microwave endoscopy	360°	Yes	N/A

[1] The field of view depends on the colonoscope it is attached to.

The proposed acquisition system has to adapt and be robust to established colonoscopy clinical practice, which entails a series of peculiarities with respect to previous microwave imaging systems reported in the literature [21], [22]. As an advantage, there is no need to penetrate the body since polyps are superficial lesions. However, a number of challenges have emerged. On one hand, space restrictions limit the number of antennas in the array, reduce the size and thickness of each antenna element and increase the mutual coupling between them. Electrically small antennas are narrowband, limiting the range of imaging algorithms to frequency domain algorithms. On the other hand, the antennas are distributed in a circular array enclosed by the imaging region instead of the imaging region being surrounded by the antennas, which is the usual configuration for microwave imaging. Finally, the unknown and changing distance from the imaging region with respect to the antenna array increases the degrees of freedom introduced by the uncertainty of the spatial and temporal delay reception of the scattered fields. Therefore, calibration methods to eliminate all unwanted effects other than the target (the polyp) are essential.

The microwave endoscopy system is verified with a colon phantom that allows to simulate a colonoscopy exploration. The phantom models a section of colon and is composed of gelatin-oil-based materials to mimic the dielectric properties of healthy colon mucosa and polyps. The reconstructed images from the phantom are quantitatively analyzed in terms of efficacy for different calibration methods.

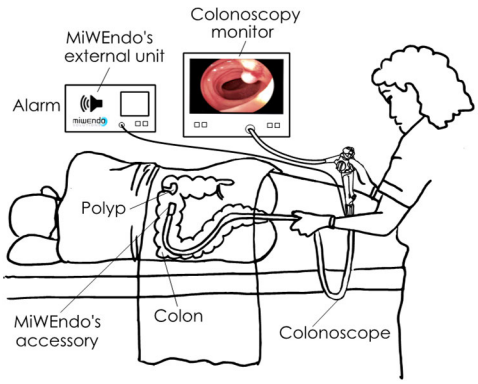

FIGURE 1. MiWEndo's microwave endoscopy system is composed of an accessory attachable at the distal tip of a standard colonoscope and an external processing unit. MiWEndo generates an alarm when a polyp is detected to warn the endoscopist.

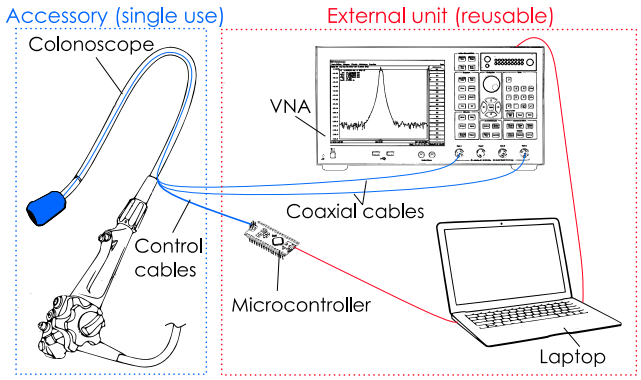

FIGURE 2. The Imaging system consists of a cylindrical ring-shaped acquisition device (in blue in the picture) attached to the end of a colonoscope and connected via cables to the external unit. The external unit consists of a vector network analyzer, a microcontroller, and a laptop.

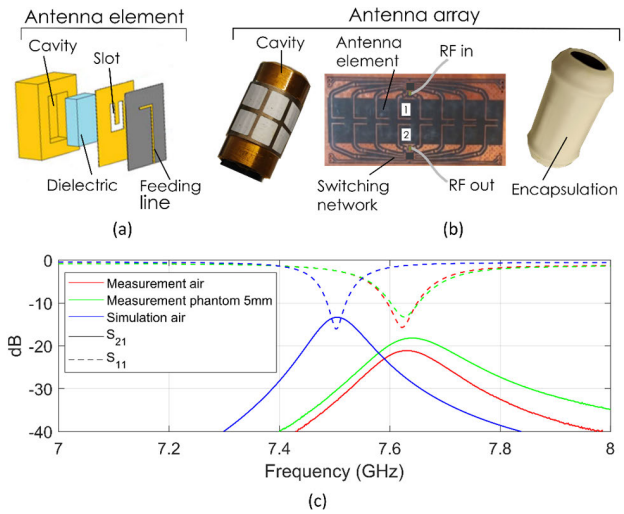

FIGURE 3. Antenna array: (a) The antenna element is a cavity-backed slot antenna; (b) The antenna array is composed by two rings of eight antennas mounted on a flexible substrate, wrapped on a cylindrical metallic cavity and protected by a plastic encapsulation; (c) Comparison between the measured and simulated reflection and the transmission coefficients in air and with a phantom.

II. MICROWAVE ENDOSCOPY SYSTEM

The imaging system consists of a combination of hardware and software components. The hardware is composed of: 1) a cylindrical ring-shaped acquisition device designed to be attached to the tip of a conventional colonoscope and 2) an external unit with a microwave transceiver, and controlling and processing units. The acquisition device is connected via cables to the external unit. The acquisition device contains two switched arrays of eight antennas organized in two rings, with one containing the transmitting antenna and the other containing the receiving antenna fed by microstrip lines. The antenna arrays are multiplexed by a two single-pole-eight-throw (SP8T) radiofrequency switches. The external unit is composed by a 2-port vector network analyzer (VNA) Keysight E5071C, a microcontroller Arduino Nano and a laptop. The VNA generates and receives the microwave signals to obtain the S-parameters and is connected to a laptop that controls the measurement. The microcontroller translates the switches' control sequences to two 3 bit codes of 0-5 V signals. Two slim coaxial cables with a diameter of 1.13 mm and a length of 500 mm transmit the microwave signals, and eight copper cables transmit the switches' control signals. Miniature connectors are used for a non-bulky final assembly. Fig. 1 shows how the microwave endoscopy system will work in clinical practice, and Fig. 2 shows the block diagram of the proposed system.

The antenna elements are cavity-backed slot antennas, as described in our previous paper [23], and are shown in Fig. 3(a). The antennas have been assembled onto a polyamide flexible printed circuit board that contains the microstrip feeding lines and the two radiofrequency switches. This assembly is wrapped around a cylindrical metallic 3D printed ring that has 16 cavities on its surface to house the antennas. The colonoscope tip can be inserted into the ring hole. The printed circuit board is covered with an encapsulation made of a biocompatible heat shrink tubing to protect the circuit from moisture and the patient from lesions. The final dimensions of the acquisition device are 30 mm in length by 20 mm in diameter, with a total thickness of 3 mm. The dimensions and shape of the device ensure non-obstruction of the front tip of the colonoscope, avoids camera concealment, injures the patient, or hinders the maneuverability of the colonoscope.

Fig. 3(c) shows the transmission and reflection coefficients measured and simulated with the central pair of transmitting and receiving antennas in the array (indicated in Fig. 3(b)). We compared the S-parameters in air with a phantom of healthy mucosa tissue situated at 5 mm from the antenna surface. In air, the antennas operate over the band 7.6-7.66 GHz, which is an approximately 0.8% fractional bandwidth with respect to the center frequency of 7.63 GHz, assuming a -10 dB reflection coefficient as a reference. The reason for such a small bandwidth is the miniaturization of the antennas ($0.12\lambda \times 0.16\lambda$). Since the antennas are very close one another, the mutual coupling increases, introducing error into the measured scattered field. Cavity-backed antennas

have been used to minimize coupling to −13 dB. The comparison between the measured and simulated results in free space shows a slight frequency shift and increased losses in the measured results. The main difference between the simulated and the measured results is the higher losses in the measurement, which are clearly seen on both the reflection and transmission S-parameters. These losses are mainly produced by the metallization roughness and welding, which is not considered in the simulation. By comparing the measurements in air with the measurements with the phantom, we can observe that the presence of the phantom affects both the transmission and reflection parameters; in fact, the input impedance matching is improved while the resonant frequency is almost the same. To obtain the measurement results at the antenna plane and remove the effects of the long cables, a Thru, Reflect, Line (TRL) calibration is used.

III. MEASUREMENT SETUP

A. COLON PHANTOM WITH POLYPS

The colon is the last part of the gastrointestinal tract. It has a segmented appearance due to a series of folds called haustra, and it is approximately 1,500 mm long and 40-90 mm in diameter. Polyps are slow-growing overgrowths of the colonic mucosa protruding into the lumen. When a colonoscopy is performed, the colon lumen is expanded using carbon dioxide insufflation. To model a colon during colonoscopy, we built a phantom with the anatomical and electrical properties of an expanded human colon. Our phantom is composed of a colon lumen model made of expanded polystyrene 268 mm in length and 66.7 mm in diameter, as shown in Fig. 4. The colon lumen was placed in the center of a cylindrical methacrylate container that was 300 mm in length and 150 mm in diameter. Expanded polystyrene has the same dielectric properties as air, making it an excellent model for the colon lumen. The polystyrene surface is undulated to simulate colon haustra and contains 4 holes to place polyps at different positions. The space between the colon lumen model and the external container walls is filled with a gelatin-oil mixture mimicking the dielectric properties of healthy mucosa tissue. The polyp is composed of a gelatin-oil mixture mimicking the dielectric properties of an adenomatous polyp with high-grade dysplasia (HGD) tissue [18].

The recipe for the healthy colon mucosa and high-grade dysplasia polyps was adapted from oil-gelatin phantoms developed for breast phantoms [24]. Oil-gelatin phantoms are low-cost, easy to produce, and nontoxic, and it is easy to change their dielectric properties by modifying the proportion of oil and water. In this case, we increased the amount of water to produce the high dielectric properties of healthy colon mucosa and polyps. In addition, some steps have been added to the original protocol [24] to produce large, high quality batches of material. First, the gelatin was hydrated with cold deionized water to completely dissolve the gelatin and

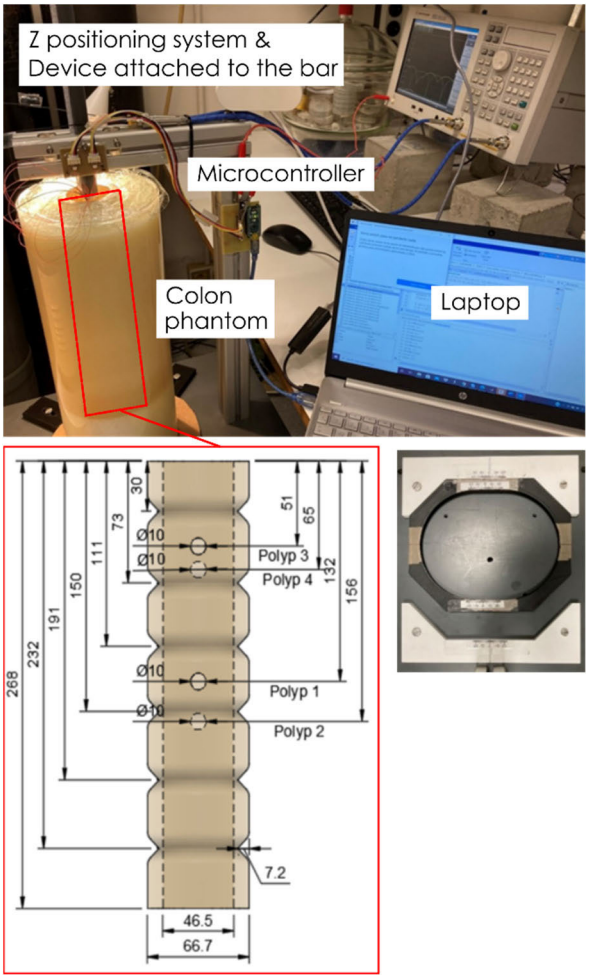

FIGURE 4. Measurement setup. The acquisition device is attached to the tip of a plastic bar. The colon phantom was placed on a 3D positioning system. The colon phantom was composed of tissue-mimicking materials poured in a methacrylate cylindrical box and an expanded polystyrene colon lumen model. The external microwave transceiver, controlling and processing unit was composed of a vector network analyzer (VNA), a microcontroller, and a laptop.

improve the homogeneity of the final mixture. To increase the velocity of polymerization and avoid the deposition of solids, the mixture was stirred continuously in a cold water bath until their temperature fell to 29 °C. Then the healthy mucosa material was poured into the phantom container between the container walls and the colon lumen polystyrene model until the container was completely filled avoiding the air gaps. Finally, the container was hermetically sealed with a silicone lid to avoid dehydration. The polyp material was poured in a small plastic airtight container. Both materials were stored in a refrigerator until they were completely solid. Before each use of the phantom, we extracted a spherical portion of 10 mm of polyp material and introduced it into the hole of the colon lumen polystyrene model. After each use, the phantom was stored in a refrigerator and completely sealed. The composition of the phantom mixtures is summarized in Table 2. No preservatives were added.

TABLE 2. Composition of the phantom mixtures.

Ingredient	Healthy mucosa	Polyp
Deionized water (ml)	3260.76	108.12
Gelatin 250 bloom (g)	326.62	10.83
Sunflower oil (ml)	1221.43	20.40
Dishwasher liquid (ml)	182.76	6.06

The dielectric properties of the tissue-mimicking phantoms were measured using the Keysight N1501A Dielectric slim form Probe Kit with the N1500A Materials Measurement Software Suite connected to a vector network analyzer Keysight E5071C. The dielectric properties of the phantom were measured before each use to track any degradation. The healthy mucosa phantom remained stable over the 30 days in which the explorations were performed, whereas the polyp phantom was redone every 15 days. The preservation of large batches of material without air contact was much longer than the preservation of the same material in smaller containers and with an air contact surface. Fig. 5 presents the relative permittivity and conductivity of the tissue-mimicking phantoms corresponding to healthy colon mucosa and polyps with high grade-dysplasia between 5-10 GHz. The dielectric properties of the phantom are compared to the measured dielectric properties of the corresponding human tissues by Guardiola *et al.* [18] and the dielectric properties of healthy colons from the IT'IS Database [25]. It can be observed that the dielectric properties of the tissue-mimicking materials reproduce both the contrast between the relative permittivity and the conductivity of the human tissue dielectric properties at 7.6 GHz.

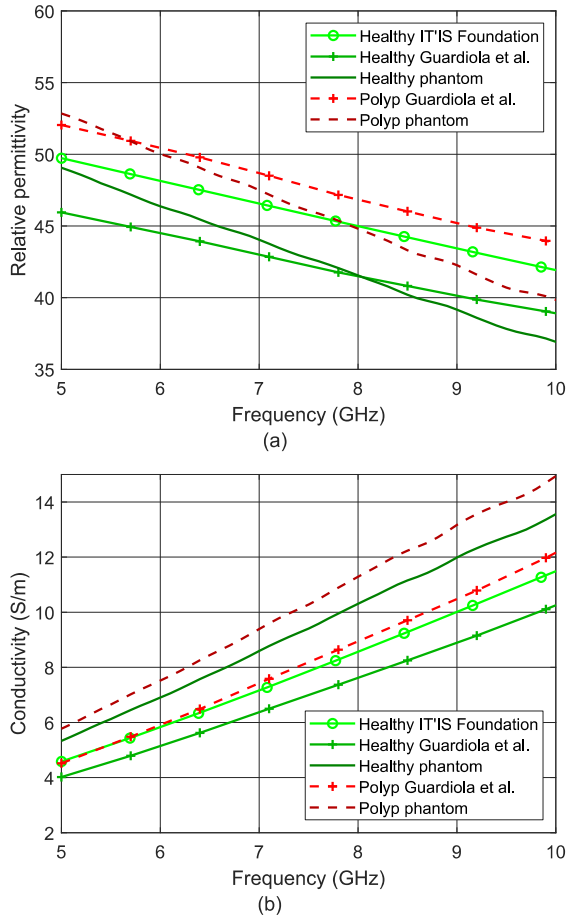

FIGURE 5. Measured dielectric properties of the phantom compared to the real patient tissues over the frequency. Polyps are unhealthy targets, and the colon mucosa is healthy tissue: (a) Relative permittivity; (b) Conductivity.

B. MEASUREMENT SETUP

To be able to reproduce a realistic colonoscopy exploration while the position of the acquisition device is known, a 3D positioning system was built (see Fig. 4). The measurement setup is composed of an L-shaped metallic structure fixed on a plastic base. The metallic structure holds a plastic bar equipped with a ruler. The acquisition device is then attached at the tip of the plastic bar. With this bar, the device is introduced vertically inside the colon lumen model. The colon phantom is placed on a mobile platform that allows movement along the x and y directions, while the plastic bar vertically allows movement of the acquisition device along the z direction. In this way, a complete positioning system in three dimensions is achieved, enabling any trajectory inside the colon phantom to be performed.

IV. DETECTION ALGORITHM

Microwave imaging is based on illuminating the object under test, the phantom, with incident radiation, E^i, and measuring the total received fields, E^t, resulting from the interaction of the incident radiation and the body under test. Data for the imaging are obtained by scanning the object from all directions. The total received field is the superposition of the incident field and the scattered field, E^s, which contains the information of the spatial changes of the dielectric properties of the phantom. By processing the total field with an imaging algorithm, the dielectric property contrast of the phantom can be reconstructed.

A. ACQUISITION ALGORITHM

Prior to the measurement, the VNA was calibrated up to the point of antenna feeding connection. The standard VNA calibration system including open-short-load connections was adopted. Since the acquisition device will be provided as a disposable set that includes the antenna array, the switching network and the cables, the VNA calibration only eliminates the effects of the VNA. Hence, the effect of slim and long coaxial cables remains and reduces the efficiency of the system. The software is a MATLAB code running on a laptop that performs 5 steps: i) establishes the connection between the VNA and the microcontroller and configures the measurement (bandwidth of 350 MHz, $N_f = 801$ frequency points, transmitting power of -5 dBm), ii) selects one transmitting and one receiving antenna pair, iii) sends the transmitting and receiving antenna selection code to the

TABLE 3. Trajectory characteristics.

#	Polyp	Num. frames	Description
1	3	49	Uniform, in front of polyp $x_i = 0, y_i = -8$
2	3	49	Uniform, further from polyp $x_i = 0, y_i = -6$
3	3	45	Uniform, further from polyp $x_i = 0, y_i = -3$
4	2	27	Uniform, centered $x_i = y_i = 0$
5	3	49	Uniform, centered $x_i = y_i = 0$
6	3	44	Uniform, centered $x_i = y_i = 0$
7	3	49	$x_i = y_i$ varying
8	3	49	Uniform, centered $x_i = y_i = 0$ with attenuators (32 dB)

microcontroller, iv) sends a trigger signal to the VNA to start the measurement of the transmitting coefficient between active antennas along the selected frequency band, v) reads the measured data from the VNA, vi) repeats ii-v until the data from all the antenna combinations are measured, vii) moves the acquisition device to the next position of the trajectory using the positioning system to obtain data from the next colon cross-section. The collected data is then stored for processing. In total, 24 combinations of transmission S-parameters (S21) are measured for each step of the trajectory. These combinations are obtained by alternatively selecting for each transmitting antenna the three closest receiving antennas, which are the adjacent, antenna and the two diagonal antennas.

To simulate a colonoscopy with the phantom, we have taken as a reference a real colonoscopy trajectory [26]. A trajectory refers to the (x, y, z) coordinates of the centroid of the acquisition cylindrical device, where the XY-plane is a horizontal or cross-sectional plane of the colon lumen, and z is the vertical coordinate. The origin of coordinates (0, 0, 0) is defined when the device is situated at the center of the cross-sectional plane of the colon lumen and the center of the 2 antenna rings is at the same height as the top base of the colon lumen (see Fig. 6). Each step of the trajectory is called a frame, $E^t_{z_i}(\vec{r}, f)$, where i is the index of the current frame. Each frame of the trajectories is separated 4 mm from the subsequent frame along the z-axis. For each frame, a $N_a \times 3 \times N_f$ matrix is obtained, where $\vec{r} = (x, y)$ and $N_a = 8$ is the number of transmitting and receiving antennas. In this study, eight different trajectories in the colon phantom with a 10-mm pedunculated polyp with HGD were measured. Table 3 summarizes the main trajectory characteristics.

B. IMAGING ALGORITHM

For each step of the trajectory, the following steps are conducted: i) calibrate the data to remove any error due to the movement of the device and the colon wall effect, ii) focus the data to obtain the reconstructed image of the dielectric contrast profile, iii) evaluate the threshold to identify whether or not there is a polyp, iv) repeat i-iii for each step of the trajectory, and v) calculate the overall sensitivity and specificity of the detection algorithm for the trajectory. The reconstruction has been done at a single frequency of $f = 7.6$ GHz.

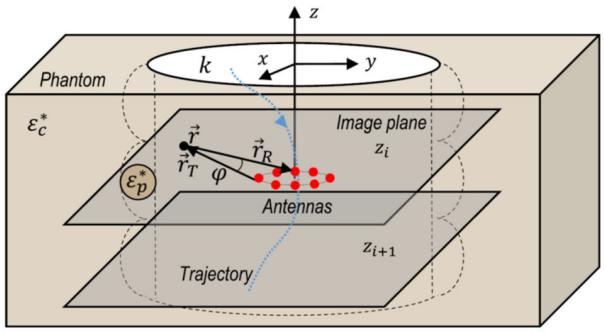

FIGURE 6. Trajectory described by the antenna array along the colon phantom.

1) CALIBRATION

Calibration consists of isolating solely the scattered field from the polyp, therefore removing any other effect. In our case, the main effect that contaminates the desired signal is the movement of the device and the colon, and thus the effect of having the colon wall at unknown and varying distances. We propose three calibration methods that share the same principle: subtraction from the actual measured frame, a previous measurement frame or a combination of previous measurement frames. The ideal calibration consists of subtracting the scattered field measured in a phantom with a polyp and its healthy counterpart, that is, a measurement with the same phantom but without polyps. In a real situation, this type of calibration is unfeasible because the healthy version of the actual colon under test is not available.

The first calibration approach is called Healthy Average Temporal (HAT) subtraction. This calibration consists of calculating the average of the transmission coefficient matrices corresponding to healthy frames, $E^t_{z_{h,j}}(\vec{r}, f)$, and subtracting it from the current measurement frame, $E^t_{z_i}(\vec{r}, f)$. This is possible in phantom experiments because there is prior knowledge of where the polyp is, but it is not feasible in clinical settings.

$$E^s_{z_i,HAT}(\vec{r}, f) = E^t_{z_i}(\vec{r}, f) - \sum_{j=1}^{N_h} \frac{1}{N_h} E^t_{z_{h,j}}(\vec{r}, f) \tag{1}$$

where N_h is the number of healthy steps averaged.

The second calibration approach is called Average Total (AT) subtraction and consists of averaging all the trajectory measurement steps and subtracting them from each measurement frame. This method is based on the hypothesis that in a colonoscopy, the vast majority of frames are healthy.

$$E^s_{z_i,AT}(\vec{r}, f) = E^t_{z_i}(\vec{r}, f) - \sum_{i=1}^{N_z} \frac{1}{N_z} E^t_{z_i}(\vec{r}, f) \tag{2}$$

where N_z is the total number of steps.

The last method is called the Hop and N Average Temporal (HNAT) subtraction. The idea behind this method is to skip the N closest frames to the current frame. The reason to skip frames from the calibration is to avoid including the effect

of the polyp if N is chosen conveniently. In this case, the scattered field produced by the polyp is estimated as:

$$E^s_{z_i,HNAT}(\vec{r},f) = E^t_{z_i}(\vec{r},f) - \sum_{j=i-H}^{i-H-N} \frac{1}{N} E^t_{z_j}(\vec{r},f) \quad (3)$$

where H is the number of steps that includes the leap and N is the number of steps that are averaged.

2) FOCUSING

Due to the small distances between the antennas and the colon wall, the information captured by the antennas is from a narrow region around the antennas. Therefore, a two-dimensional electromagnetic analysis can be performed. Considering the constraints of the system, two versions of a frequency domain imaging algorithm are implemented, namely, Bifocusing (B) and Modified Monofocusing (MM); see equations (4) and (5), respectively. These algorithms form every image point of the dielectric property contrast of the colon by creating one or two focused groups of antennas (one for the transmitters and the other for the receivers). The received scattered field from each antenna pair is numerically weighted with a focusing operator in order to be focused on a unique point in the reconstruction grid. The focusing operator restores the module and phase changes suffered by a wave on its way to and/or from every image point. For each image point, the coherent summation of all the scattering focused fields from all antenna combinations results in a large intensity value if the actual point is the origin of the scattering (polyp). If not, the summation results in a small value, and this contribution can be considered noise. Note that we assumed that the z-coordinates of the transmitting and receiving rings of antennas are the same; thus, their positions are denoted as $\vec{r}_T = (x_T, y_T)$ and $\vec{r}_R = (x_R, y_R)$, respectively.

$$I^B_{z_i}(\vec{r}) = \left| \sum_{k=(j-1)_{N_a}}^{(j+1)_{N_a}} \sum_{j=1}^{N_a} \frac{E_s(\vec{r}_{T_j}, \vec{r}_{R_k}, z_i)}{k^2 H_0^2(k\,|\vec{r}_{T_j} - \vec{r}|) H_0^2(k\,|\vec{r}_{R_k} - \vec{r}|)} \right| \quad (4)$$

$$I^{MM}_{z_i}(\vec{r}) = \left| \sum_{k=(j-1)_{N_a}}^{(j+1)_{N_a}} \sum_{j=1}^{N_a} E_s^2\left(\vec{r}_{T_j}, \vec{r}_{R_k}, z_i\right) J_1^2 \times \left(k\,|\vec{r}_{R_k} - \vec{r}|\right) e^{j2(k|\vec{r}_{R_k} - \vec{r}| + \varphi)} \right| \quad (5)$$

where $k = 2\pi f$ is the wavenumber and φ is the angle between the transmitting and receiving antennas.

3) THRESHOLDING

For each reconstructed image frame, $I_{z_i}(\vec{r})$, the thresholding method compares the maximum of the current reconstruction with the average maximum of the previous reconstructed images that have been classified as healthy, $I_{z_{h,j}}(\vec{r})$. If the quotient of those values is higher than the detection threshold, then the current frame is labeled as containing a polyp (6). Otherwise, the current frame is labeled as healthy and is added to the average of the healthy maximums. The first frame is always considered as healthy. For the frames labeled as containing a polyp, the system will generate an alarm.

$$\max\left\{I_{z_i}(\vec{r})\right\} \Big/ \sum_{j=1}^{N_h} \frac{1}{N_h} \max\left\{I_{z_{h,j}}(\vec{r})\right\} > \text{threshold} \quad (6)$$

Finally, the overall performance of the system to detect polyps in all trajectories is evaluated using the sensitivity and specificity. The sensitivity, also called the true positive (TP) rate, measures the percentage of cases having a polyp that are correctly diagnosed as having the lesion. A false negative (FN) occurs when a negative result is reported to a trajectory that does have a polyp. The specificity, also called the true negative (TN) rate, measures the percentage of healthy cases that are correctly identified as not having any polyp. A false positive (FP) is reported when the test wrongly indicates that a polyp is present. The values of sensitivity and specificity are related to the TP, FP, TN, and FN values through the following equations:

$$\text{sensitivity} = \frac{TP}{TP + FN} \quad (7)$$

$$\text{specificity} = \frac{TN}{TN + FP} \quad (8)$$

V. RESULTS

We measured and reconstructed the eight trajectories described in Table 3 using the different calibration methods. As an example, Fig. 7 shows the evolution of the normalized maximum amplitude of the reconstructed image registered in each step of the trajectory. The trajectories analyzed in Fig. 7 correspond to Trajectory 1 and Trajectory 7, where the polyp is between frames [44, 47] and [41, 44], respectively. The raw measured transmission coefficients for each antenna combination were calibrated using three different strategies: Average Total subtraction, Hop and N Average Temporal subtraction and Healthy Average Temporal subtraction. These will now be referred to as AT, HNAT and HAT, respectively. The first two strategies intend to emulate the results of the HAT, which is an ideal and non-realistic calibration. For each calibration strategy, the image was created using both Bifocusing and Modified Monofocusing focusing algorithms. The movement along the y-axis of the device, or the distance to the polyp, has also been included in the plots to analyze the relation between the device's displacement and the reconstruction. Vertical continuous orange lines indicate the limits of colon haustrum, and vertical continuous red lines indicate the limits of the polyp.

The maximum reconstructed amplitude represented in Fig. 7 has been normalized between 0 and 1, using the maximum amplitude of each calibration set, in order to enable a better comparison between the different methods and trajectories. It is possible to appreciate that the evolution of the maximum registered along the trajectory reveals an identical tendency for the three different calibration strategies and for

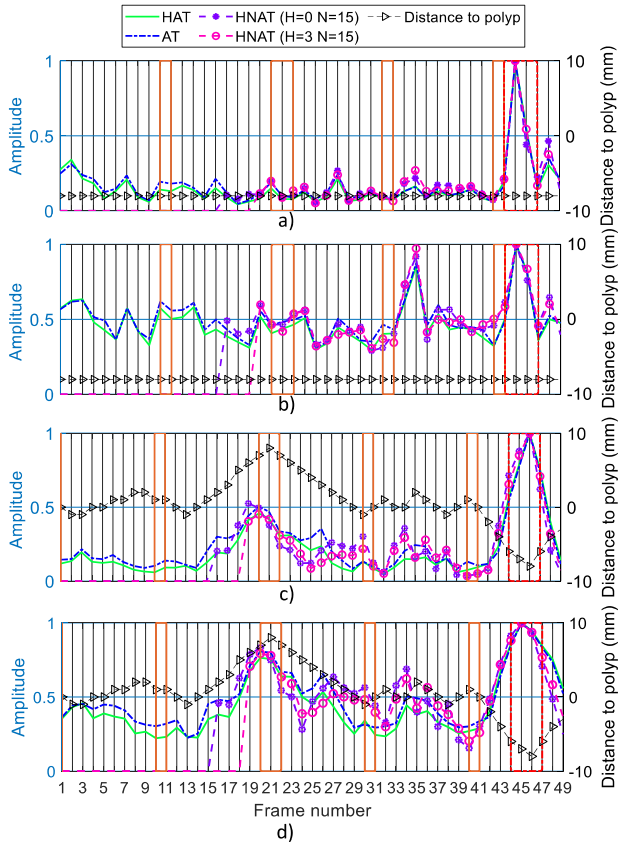

FIGURE 7. Evolution of the normalized maximum reconstructed amplitude for different calibrations: a) Trajectory 1 using Modified Monofocusing; b) Trajectory 1 using Bifocusing; c) Trajectory 7 using Modified Monofocusing; and d) Trajectory 7 using Bifocusing algorithm.

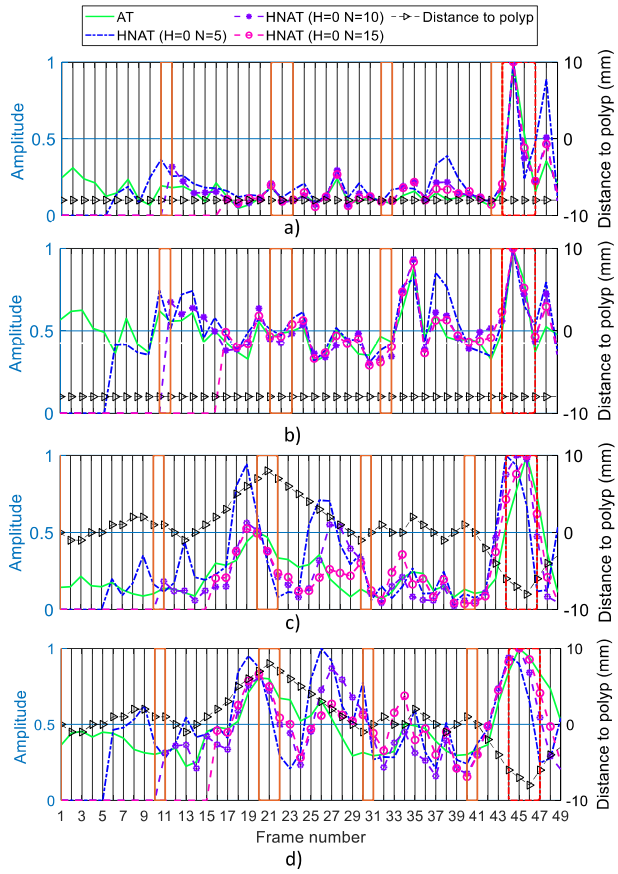

FIGURE 8. Evolution of the normalized maximum reconstructed amplitude for HNAT calibration using different N and H parameters: a) Trajectory 1 using Modified Monofocusing; b) Trajectory 1 using Bifocusing; c) Trajectory 7 using Modified Monofocusing; and d) Trajectory 7 using Bifocusing algorithm.

the two focusing algorithms, i.e., Modified Monofocusing and Bifocusing. Indeed, the absolute maximum of all the traces displayed in Fig. 7 corresponds to the position of the polyp. Local maximums are also observed when the trajectory approaches the colon walls. Haustrum does not seem to produce any effect on the reconstructed results.

Concerning the calibration strategies, both AT and HNAT offer a similar performance to HAT. In the case of the HNAT strategy, the number of averaged frames (N) is set to 15, and two different sizes of the backwards leap (H) are analyzed. On one hand, H has been assigned a value of 3 since polyp diameter is always 10 mm; therefore, there are only 4 frames in which the polyp is inside the detection zone of the device. Hence, if we want to avoid including information from the polyp in the calibration set, it is necessary to omit the 3 previous frames to the frame that is actually reconstructed. Likewise, the case of $H = 0$ has also been analyzed to assess whether a sufficiently large number of averaged frames (N) could minimize the effect of the polyps during the calibration, thereby emulating the principle of the AT strategy. Fig. 8 includes the results obtained when calibrating with different N values and H=0. As shown in Fig. 8, the larger N is, the less sensitive the calibration is to noise and therefore the more robust it is. Additionally, in the frames where the polyp is detected, a larger N minimizes the contribution of the polyp in the average used to calibrate, allowing a more similar detection to the one observed with the AT strategy.

Regarding the focusing method, as shown in Fig. 7, the difference in amplitude between the frames that correspond to a healthy colon and those where the polyp is inside the detection zone of the device is higher when Modified Monofocusing algorithm is used, allowing an easier detection of the polyp using a threshold without false positives. Fig. 9 shows the cross-sectional reconstructed images using AT calibration and Modified Monofocusing and Bifocusing algorithms in the frame corresponding to the absolute maximum in Fig. 7; that is, the position of the polyp. The magnitude represented is the normalized reconstructed dielectric contrast profile at 7.6 GHz represented on a logarithmic scale between 0 and 1. The blue circle in the middle of the plots indicates the position of the device, and the red dots indicate the position of each antenna. As shown in Fig. 9, both algorithms are able to detect and locate the polyp, showing higher intensities in the position of the polyp. The Modified Monofocusing algorithm can obtain punctual

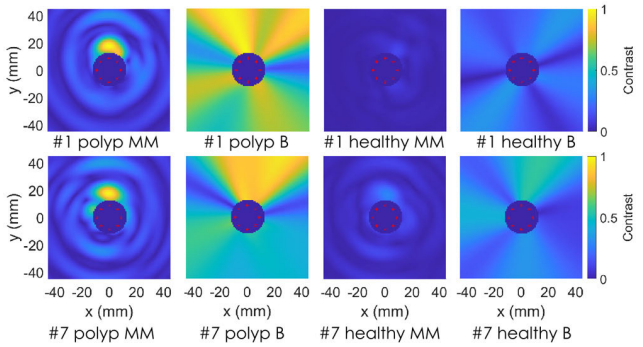

FIGURE 9. Cross-sectional reconstruction of the normalized dielectric contrast corresponding to Trajectories 1 and 7 for the frame that contains the absolute maximum amplitude of the trajectory (polyp) and a healthy frame using Bifocusing (B) and Modified Monofocusing (MM). The calibration was performed with the AT strategy.

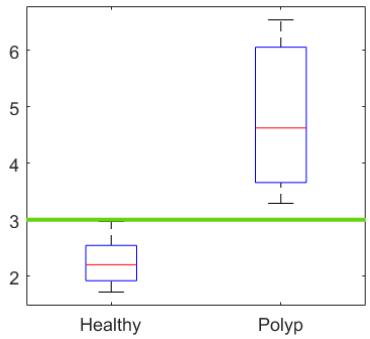

FIGURE 10. Normalized maximum reconstructed amplitude of each patient and frame for healthy mucosa and for polyps using Modified Monofocusing and HNAT. The detection threshold is represented as a green line.

detection, while Bifocusing does not obtain discrimination in the range direction.

Finally, we assess the performance of the complete detection algorithm. Seeing the previous results, we selected Modified Monofocusing as the focusing algorithm and HNAT as the calibration method. The values of N and H were selected depending on the characteristics of each trajectory. Fig. 10 shows a boxplot that represents the normalized maximum reconstructed amplitude of each patient and frame for healthy mucosa and for polyps. The blue box includes the values within the 25th and 75th percentiles and the red line is the median. The detection threshold is represented as a horizontal green line. All the values above the threshold were classified as lesions and those below as healthy mucosa. The detection thresholds were defined to optimize the specificity and sensitivity to detect polyps from healthy mucosa. True detection is considered when the maximum amplitude of a frame is higher than the threshold in at least one frame, and this frame is within the range of frames where the polyp is in front of any antenna. The results show that Modified Monofocusing combined with HNAT provides a perfect detection, fixing the threshold to 3 without false positives or false negatives. This means a specificity and sensitivity equal to 100% and ensures that no polyps are missed.

VI. DISCUSSION AND CONCLUSION

We evaluated a novel microwave-based device and used the IDEAL model to drive this innovation. In this paper, we reported on the process of conceptualization and preparation before its implementation in patients. The IDEAL Framework and Recommendations [27] represent a new paradigm for evaluating surgical operations, invasive medical devices and other complex therapeutic interventions. A miniaturized acquisition system for a microwave colonoscopy system to detect colorectal polyps with an alarm was presented in this paper. The acquisition device was designed as a switched cylindrical array of 16 antennas organized in two rings of eight antennas, each containing the transmitters and the receivers. The device was encapsulated and attached at the tip of a bar simulating a colonoscope. The antennas were switched in pairs following a predefined sequence, and the S-parameters were measured to obtain a measured frame. This process was repeated a number of steps to form a trajectory. A vector network analyzer, a microcontroller and a laptop were used for data acquisition and signal processing.

The system was designed to be compatible with colonoscopy and produce minimal changes into current clinical practice. First, concerning size restrictions, the final dimensions of the acquisition device are 30 mm in length by 20 mm in diameter, with a total thickness of 3 mm. The dimensions and shape of the device ensure non-obstruction of the front tip of the colonoscope, avoids injuring the patient or hindering the maneuverability of the colonoscope. Similar accessories in shape and size are available on the market, and in the future the accessory could be integrated into the colonoscope tube. The antenna elements show typical electrically small antenna performance, characterized by a narrow bandwidth of 60 MHz (0.8% fractional bandwidth) and an omnidirectional radiation pattern. An omnidirectional radiation pattern is suitable for this case, where we want to ensure a 360° coverage of the colon wall. Mutual coupling between adjacent antennas has been minimized to −13 dB using cavity-backed antenna design.

The system is verified with a colon phantom that simulates realistic colonoscopy exploration. The phantom models a section of a colon, including the haustrum and allows placement of different polyps. The phantom is composed of gelatin-oil based materials to mimic the dielectric properties of colon healthy mucosa and polyps with high-grade dysplasia. Once manufactured, the tissue-mimicking materials were measured with a coaxial probe, achieving dielectric properties very similar to those of real human tissues, with relative permittivities of 41 and 46 and conductivities of 9 S/m and 9.8 S/m, respectively.

The acquired data are processed with a 3-step algorithm that generates an alarm when a polyp is detected. In the first step, the scattering fields are estimated by using three different calibration methods. This is a crucial step to remove the spatial-temporal uncertainty on the reception of the scattered fields due to the unknown and changing distance

from the acquisition device and the colon wall. Next, two focusing methods are compared to obtain a cross-sectional image of each step, and finally a detector based on a threshold is used to generate the alarm.

Regarding the calibration, the most important challenge is to differentiate the effect of the device and the colon movements from the effect of the presence of the polyp, since both produce changes in the measured scattered field. This can be observed if we compare the results of Trajectory 1 and Trajectory 7 in Fig. 7. Trajectory 7 shows a smaller difference between the absolute and local maximums, suggesting that the main undesired effect that the calibration must face is device movement. This effect is evident in frames 15 to 22 of Trajectory 2; in this region, the accessory moves along the y-axis toward the colon wall. Thus, the device movement is not completely corrected with any calibration; however, the correction obtained is sufficient to achieve perfect detection of polyps in the studied cases. AT and HNAT offer a similar performance to HAT. Hence these two strategies can be used to simulate the HAT, which although it is the ideal calibration, it is unrealistic since it depends on prior knowledge of healthy frames, which is knowledge that is not available in a clinical scenario. AT offers similar results to HAT if the percentage of frames with polyp vs. healthy frames is less than 10%. HNAT seems to be the most suitable calibration in a real case, even though the first $N+H$ frames cannot be calibrated nor analyzed. Moreover, the selection of N values is a key, as the larger N is, the better the results, but the greater the calibrated detection is delayed. In this paper, the selection of these values was performed manually; however, in a realistic scenario it must be done automatically. To do so, more trajectories in phantoms of different shapes will be studied.

Regarding the focusing method, Modified Monofocusing presents better results while avoiding false positives in regions with large movements. Moreover, Modified Monofocusing presents focused detection with fewer artifacts, whereas Bifocusing is only able to focus on an angular section. The main reason for this lack of range resolution is the narrow frequency band of the antennas. However, this is not a problem for our system since the output is only an alarm. According to the opinion of more than 30 doctors with whom we have collaborated, it is not necessary for our device to provide additional information, for example, the angular position of the polyp, since it could distract the doctor's attention during colonoscopy. The unusual imaging configuration in which the antennas are surrounded by the imaging region (colon) causes there to be no direct vision between half of the array antennas and the focusing point since the signal cannot pass through the device. For this reason, focusing based on re-establishing the effect produced in the fields due to the distance between an image point and the transmitting and receiving antennas is wrong for these antenna combinations. This effect has been reduced by only including the three closest receiving antennas for each transmitter in the reconstruction. The residual error produced by this effect is translated into artifacts in the reconstructed image, especially appearing with the Bifocusing method. Moreover, due to the narrowband behavior of the antennas, we cannot benefit from a frequency averaging, which is commonly used to cancel the frequency selective artifacts [28].

Finally, it has been observed that it is possible to define a fixed threshold that would enable perfect detection of the polyp in all of the studied trajectories. Notwithstanding, more trajectories must be tested, and more sophisticated thresholding methods will be designed to make the threshold more robust.

Eight different trajectories were measured to assess different detection challenges of this application:

1) The phantom includes six folds to study the effect of colon folds. We have shown that the folds do not produce false positives in any of the trajectories made with this phantom.
2) Two polyp positions were considered: Polyp 2 was in between colon folds, and Polyp 3 was just behind a fold. A polyp behind a fold is difficult to detect with conventional colonoscopy because the camera only has frontal vision. We demonstrated with Trajectory 4 that a polyp behind a fold can be detected.
3) The movement of the colonoscope, and hence the unknown distance between the antenna and the colon, was studied with Trajectory 7. We demonstrated that the developed calibration is able to reduce this effect to allow detection.
4) Repeatability. Three uniform and centered trajectories (4, 5, 6) were performed, and we obtained very similar results.
5) Attenuation. We studied the capacity to detect polyps at different distances with Trajectories 1, 2, and 3. In Trajectory 8, we included 16 dB attenuators between the VNA ports and the coaxial cable. Therefore, with a total additional attenuation of 32 dB detection is still possible. The reason to do so is to simulate the losses expected for the 2 m coaxial cables that will be used in the final system.

The main limitation of this study is that the phantom does not include angulations. The ability to detect polyps of different sizes and shapes (sessile and flat) has also not been studied. Therefore, further studies with a colon lumen model extracted from patient computed tomography colonography will be manufactured, measured and reconstructed in future experiments.

In summary, this study demonstrated for the first time the use of a microwave-based device to be used as an accessory of a standard colonoscope to detect polyps in a phantom.

REFERENCES

[1] J. Ferlay, M. Ervik, F. Lam, M. Colombet, L. Mery, M. Piñeros, A. Znaor, I. Soerjomataram, and F. Bray, "Global cancer observatory: Cancer today," Int. Agency Res. Cancer, Lyon, France, 2020. Accessed: Jul. 28, 2021. [Online]. Available: https://gco.iarc.fr/today

[2] R. L. Siegel, K. D. Miller, and A. Jemal, "Cancer statistics, 2015," *CA Cancer J. Clin.*, vol. 65, no. 1, pp. 5–29, 2015.

[3] (2021). *Surveillance Research Program, National Cancer Institute SEER*Stat Software*. [Online]. Available: seer.cancer.gov/seerstat

[4] J. C. van Rijn, J. B. Reitsma, J. Stoker, P. M. Bossuyt, S. J. van Deventer, and E. Dekker, "Polyp miss rate determined by tandem colonoscopy: A systematic review," *Amer. J. Gastroenterol.*, vol. 101, no. 2, pp. 343–350, 2006.

[5] N. J. Samadder, K. Curtin, T. M. Tuohy, L. Pappas, K. Boucher, D. Provenzale, K. G. Rowe, G. P. Mineau, K. Smith, R. Pimentel, and A. C. Kirchhoff, "Characteristics of missed or interval colorectal cancer and patient survival: A population-based study," *Gastroenterology*, vol. 146, no. 4, pp. 950–960, 2014.

[6] W. N. Sing and C. Rees, "Can technology increase adenoma detection rate," *Therapeutic Adv. Gastroenterol.*, vol. 11, pp. 1–18, Jan. 2018.

[7] R. Kumashiro, K. Konishi, T. Chiba, T. Akahoshi, S. Nakamura, M. Murata, M. Tomikawa, T. Matsumoto, Y. Maehara, and M. Hashizume, "Integrated endoscopic system based on optical imaging and hyperspectral data analysis for colorectal cancer detection," *Anticancer Res.*, vol. 36, no. 8, pp. 3925–3932, 2016.

[8] G. Urban, P. Tripathi, T. Alkayali, M. Mittal, F. Jalali, W. Karnes, and P. Baldi, "Deep learning localizes and identifies polyps in real time with 96% accuracy in screening colonoscopy," *Gastroenterology*, vol. 155, no. 4, pp. 1069–1078.e8, 2018.

[9] J. E. East, B. P. Saunders, D. Burling, D. Boone, S. Halligan, and S. A. Taylor, "Surface visualization at CT colonography simulated colonoscopy: Effect of varying field of view and retrograde view," *Amer. J. Gastroenterol.*, vol. 102, no. 11, pp. 2529–2535, Nov. 2007.

[10] D. Freedman, Y. Blau, L. Katzir, A. Aides, I. Shimshoni, D. Veikherman, T. Golany, A. Gordon, G. Corrado, Y. Matias, and E. Rivlin, "Detecting deficient coverage in colonoscopies," *IEEE Trans. Med. Imag.*, vol. 39, no. 11, pp. 3451–3462, Nov. 2020.

[11] N. K. Nikolova, *Introduction to Microwave Imaging*. Cambridge, U.K.: Cambridge Univ. Press, 2017.

[12] P. M. Meaney, D. Goodwin, A. H. Golnabi, T. Zhou, M. Pallone, S. D. Geimer, G. Burke, and K. D. Paulsen, "Clinical microwave tomographic imaging of the calcaneus: A first-in-human case study of two subjects," *IEEE Trans. Biomed. Eng.*, vol. 59, no. 12, pp. 3304–3313, Dec. 2012.

[13] S. Y. Semenov, V. G. Posukh, A. E. Bulyshev, T. C. Williams, Y. E. Sizov, P. N. Repin, A. Souvorov, and A. Nazarov, "Microwave tomographic imaging of the heart in intact swine," *J. Electromagn. Waves Appl.*, vol. 207, no. 7, pp. 873–890, 2006.

[14] M. Shere, I. Lyburn, R. Sidebottom, H. Massey, C. Gillett, and L. Jones, "MARIA m5: A multicentre clinical study to evaluate the ability of the micrima radio-wave radar breast imaging system (MARIA) to detect lesions in the symptomatic breast," *Eur. J. Radiol.*, vol. 116, pp. 61–67, Jul. 2019.

[15] D. O'Loughlin, M. O'Halloran, B. M. Moloney, M. Glavin, E. Jones, and M. A. Elahi, "Microwave breast imaging: Clinical advances and remaining challenges," *IEEE Trans. Biomed. Eng.*, vol. 65, no. 11, pp. 2580–2590, Nov. 2018.

[16] L. Crocco, I. Karanasiou, M. L. James, and R. C. Conceição, *Emerging Electromagnetic Technologies for Brain Diseases Diagnostics, Monitoring and Therapy*. Cham, Switzerland: Springer, 2018.

[17] O. Karadima, M. Rahman, I. Sotiriou, N. Ghavami, P. Lu, S. Ahsan, and P. Kosmas, "Experimental validation of microwave tomography with the DBIM-TwIST algorithm for brain stroke detection and classification," *Sensors*, vol. 20, no. 3, p. 840, 2020.

[18] M. Guardiola, S. Buitrago, G. Fernández-Esparrach, J. M. O'Callaghan, J. Romeu, M. Cuatrecasas, H. Córdova, M. Á. G. Ballester, and O. Camara, "Dielectric properties of colon polyps, cancer, and normal mucosa: *Ex vivo* measurements from 0.5 to 20 GHz," *Med. Phys.*, vol. 45, no. 8, pp. 3768–3782, Aug. 2018.

[19] W. S. Ngu, R. Bevan, Z. P. Tsiamoulos, P. Bassett, Z. Hoare, M. D. Rutter, G. Clifford, N. Totton, T. J. Lee, A. Ramadas, J. G. Silcock, J. Painter, L. J. Neilson, B. P. Saunders, and C. J. Rees, "Improved adenoma detection with endocuff vision: The ADENOMA randomised controlled trial," *Gut*, vol. 68, no. 2, pp. 280–288, Feb. 2019.

[20] A. Repici, M. Badalamenti, R. Maselli, L. Correale, F. Radaelli, E. Rondonotti, E. Ferrara, M. Spadaccini, A. Alkandari, A. Fugazza, A. Anderloni, P. A. Galtieri, G. Pellegatta, S. Carrara, M. Di Leo, V. Craviotto, L. Lamonaca, R. Lorenzetti, and C. Hassan, "Efficacy of real-time computer-aided detection of colorectal neoplasia in a randomized trial," *Gastroenterology*, vol. 159, no. 2, pp. 512–520, 2020.

[21] M. Klemm, I. J. Craddock, J. A. Leendertz, A. Preece, and R. Benjamin, "Radar-based breast cancer detection using a hemispherical antenna array—Experimental results," *IEEE Trans. Antennas Propag.*, vol. 57, no. 6, pp. 1692–1704, Jun. 2009.

[22] B. J. Mohammed, A. M. Abbosh, S. Mustafa, and D. Ireland, "Microwave system for head imaging," *IEEE Trans. Instrum. Meas.*, vol. 63, no. 1, pp. 117–123, Jan. 2014.

[23] M. Guardiola, K. Djafri, M. Challal, M. A. Gonzalez Ballester, G. Fernandez-Esparrach, O. Camara, and J. Romeu, "Design and evaluation of an antenna applicator for a microwave colonoscopy system," *IEEE Trans. Antennas Propag.*, vol. 67, no. 8, pp. 4968–4977, Aug. 2019.

[24] S. Di Meo, L. Pasotti, I. Iliopoulos, M. Pasian, M. Ettorre, M. Zhadobov, and G. Matrone, "Tissue-mimicking materials for breast phantoms up to 50 GHz," *Phys. Med. Biol.*, vol. 64, no. 5, Feb. 2019, Art. no. 055006.

[25] P. A. Hasgall *et al.*, "IT'IS database for thermal and electromagnetic parameters of biological tissues," May 2018. Accessed: Jul. 28, 2021. [Online]. Available: https://itis.swiss/virtual-population/tissue-properties/database/dielectric-properties/

[26] K. G. V. J. Jayender and R. S. J. Estepar, "New kinematic metric for quantifying surgical skill for flexible instrument manipulation," in *Proc. 1st Int. Conf. Inf. Process. Comput.-Assist. Intervent. (IPCAI)*, Geneva, Switzerland, Jun. 2010, pp. 81–90, doi: 10.1007/978-3-642-13711-2_8.

[27] *IDEAL Collaboration*. Accessed: Jul. 28, 2021. [Online]. Available: https://www.ideal-collaboration.net/

[28] L. Jofre, A. Broquetas, J. Romeu, S. Blanch, A. P. Toda, X. Fabregas, and A. Cardama, "UWB tomographic radar imaging of penetrable and impenetrable objects," *Proc. IEEE*, vol. 97, no. 2, pp. 451–464, Feb. 2009.

ALEJANDRA GARRIDO received the degree in engineering and the master's degree in telecommunications from the Universitat Politècnica de Catalunya, Barcelona. She has been working on microwave systems and antenna design, since 2018, as a part-time Research Assistant at Comsenslab (UPC). In 2018, she completed her stay at Aalto University, Finland, designing integrated antennas for green buildings. She is currently working as a Software Engineer with MiWEndo Solutions. She has coauthored four scientific articles. She has experience working in machine learning and computer vision.

ROBERTO SONT received the degree in telecommunications engineering and the master's degree in telecommunications from the Universitat Politècnica de Catalunya, Barcelona, in 2017 and 2019, respectively. He is currently a Hardware Engineer with MiWEndo Solutions. He has developed a measurement system for Zanini Auto Group to characterize radomes in the automotive sector as a final degree project.

WALID DGHOUGHI received the degree in biomedical engineering with a major in medical imaging and the M.Sc. degree in biomedical engineering from UPM, and the master's degree in technological innovation in health programme (EIT Health). He is highly enthusiast about technological innovation and a strong believer in the role of engineering in the progress of medicine. He is trained in innovation and entrepreneurship, AI, and eHealth.

SERGI MARCOVAL received the bachelor's degree in biomedical engineering from Universitat Pompeu Fabra, in 2021. In 2020, he performed an Erasmus Program at the Politecnico di Milano, Italy. He is passionate about medical devices, especially those related to minimally invasive diagnosis and therapies. He is currently working in preclinical validation and regulatory affairs with MiWEndo Solutions.

JORDI ROMEU (Fellow, IEEE) was born in Barcelona, Spain, in 1962. He received the Ingeniero de Telecomunicación and Doctor Ingeniero de Telecomunicación degrees from the Universitat Politècnica de Catalunya (UPC), in 1986 and 1991, respectively. In 1985, he joined the Antenna Laboratory, Signal Theory and Communications Department, UPC, where he is currently a Full Professor, and involved in antenna near-field measurements, antenna diagnostics, and antenna design. He was a Visiting Scholar with the Antenna Laboratory, University of California at Los Angeles, Los Angeles, in 1999, on a NATO Scientific Program Scholarship, and the University of California at Irvine, in 2004. He holds several patents and has published 60 refereed articles in international journals and 80 conference proceedings. He was the Grand Winner of the European IT Prize, awarded by the European Commission, for his contributions in the development of fractal antennas, in 1998 (more information can be found at http://www.researchgate.net/profile/Jordi-Romeu).

GLÒRIA FERNÁNDEZ-ESPARRACH received the M.D. degree from the University of Barcelona, in 1988, and the Ph.D. degree in 1997. She was a Diplomate of Spanish Board of Gastroenterology. She has been a Professor with the University of Barcelona, since 2015. With more than 20 years of experience in clinical practice as an Endoscopist at HCB, in the last ten years, she has focused her activity on therapeutic endoscopy and endoscopic ultrasonography. After a stay as a Guest Researcher at the Experimental Endoscopy Unit, Brigham and Women's Hospital, Boston, under the direction of Dr. Christopher C. Thompson, from July 2007 to June 2008, she started her own Experimental Endoscopy Laboratory, in 2009. She is currently a Researcher with IDIBAPS and CIBEREHD.

IGNASI BELDA is currently a Computer Scientist, a Doctor in artificial intelligence applied to drug discovery, and a Doctor in law and taxation. He has been the CEO of the Barcelona Science Park for two years. He has founded or co-founded six start-ups in biomedicine. He has published dozens of scientific articles, he has participated as a speaker in more than 50 international conferences and has written six outreach books about artificial intelligence and telecommunications, which have been translated into multiple foreign languages. Thanks to his entrepreneurship career, he has been awarded 20 national and international prizes, including the Award Princesa de Girona, in 2014, or the Headstart Catalyst Award, in 2020, given by the U.S. National Academy of Medicine.

MARTA GUARDIOLA has been working in microwave imaging systems for medical diagnosis with the Universitat Politècnica de Catalunya, since 2008, and the Universitat Pompeu Fabra, since 2014. She is currently an Engineer and a Doctor in telecommunications. She has authored six refereed articles in international journals and 25 conference proceedings. She holds a patent and was awarded ten prizes, including The Spinoff Prize, a Nature Research Award. Her research interests include microwave imaging algorithms, computational models and electromagnetic simulations, the design and manufacturing of microwave imaging acquisition systems, and preclinical validation.